Ocean Engineering 349 (2026) 124115

Contents lists available at ScienceDirect

Ocean Engineering

journal homepage: www.elsevier.com/locate/oceaneng

Research paper

Modeling and validation of a small heave plate wave energy converter

Hannah Walker [a,*], Michael T. Tolley [a], Geno Pawlak [a,b]

[a] UCSD, 9500 Gilman Dr, La Jolla, 92093, CA, USA
[b] Scripps Institution of Oceanography, 8622 Kennel Way, La Jolla, 92037, CA, USA

ARTICLE INFO

Keywords:
Heave plate WEC
Lumped-Parameter model
Experimental validation

ABSTRACT

Wave energy converters (WECs) are increasingly being adapted for smaller-scale applications, such as powering unmanned oceangoing vehicles. For free-floating ocean platforms, there is a need for a simplified modeling framework that can be efficiently applied and used as a foundation for future optimization and design insight.

We present the development and validation of a lumped-parameter model representative of a small heave plate WEC designed for short-period waves (1-5 s) typical of moderate wind conditions. The modeled system consists of a negatively buoyant drag plate and a surface buoy connected by a spring-damper power take-off (PTO) that captures the relative motion between the two bodies.

To validate the model, a physical prototype of the heave plate WEC was constructed. A linear actuator simulated wave excitation, replicating the idealized vertical forcing experienced by a buoy in a wave field. Experiments varied wave conditions, system mass, and PTO parameters to assess their influence on the model and measured response. Results show that lower non-dimensional spring constants (K^*) improve broadband performance, while higher non-dimensional masses (M^*) yield only marginal increases in mean power. These findings confirm the model's accuracy and provide guidance for optimizing WEC design for free-floating platforms.

1. Introduction

Wave energy converters (WECs) harness ocean wave motion to drive power-harvesting components, typically generating electricity for off-board applications (Salter, 1974; Falnes, 2007). Some oceangoing platforms, such as the Wirewalker (Del Mar Oceanographic, LLC) and the Wave Glider (Liquid Robotics, Inc.), exploit differential wave motion, harnessing energy for onboard use to drive horizontal or vertical platform movement (Daniel et al., 2011; Pinkel et al., 2010). Numerous WEC designs have been comprehensively described and reviewed by (de O., 2010; Rehman et al., 2023; Cruz, 2007). One common design is a floating small-scale heave plate WEC (Guo et al., 2022). In this study, we examine the dynamics of a small idealized heave plate WEC intended to generate electrical energy at a scale appropriate for onboard use in ocean platform applications such as for an Unmanned Underwater Vehicle (UUV). The model is designed to capture essential system dynamics while remaining computationally efficient, making it a flexible foundation for further optimization, control strategies, and design insight.

A free-floating heave plate WEC consists of a surface buoy, a submerged heave plate and a power take-off (PTO). These components are interconnected and vertically separated. Passing ocean waves vertically oscillate the surface buoy whereas the motion of the submerged heave plate is damped by nonlinear drag and added mass forces. This results in a periodic differential in motion. An optimally tuned PTO captures this motion and converts it into electrical energy.

According to linear wave theory, wave-induced pressure and velocity perturbations decay exponentially with depth at a rate determined by the surface wavelength. For maximum effectiveness, the vertical separation between the surface float and the submerged heave plate in a WEC should be selected to match the characteristic decay scale. In the deep-water limit, where the water depth is significantly greater than the wavelength ($h \gg \lambda$), the magnitude of the oscillatory differential velocity, $|w|$, between a plate located at depth z_{HP} and the free surface is expressed as

$$|w| = \frac{\pi H}{T}\left(1 - e^{-\frac{z_{HP}}{g}\left(\frac{2\pi}{T}\right)^2}\right) \tag{1}$$

where g is gravitational acceleration, H is wave height, and T is wave period (Kundu et al., 2015). This relationship guides the determination of the optimal vertical separation of components, tailored to the specific wave scales of interest.

* Corresponding author.
E-mail addresses: h2walker@ucsd.edu (H. Walker), mttolley@ucsd.edu (M.T. Tolley), epawlak@ucsd.edu (G. Pawlak).

https://doi.org/10.1016/j.oceaneng.2025.124115
Received 21 October 2025; Received in revised form 12 December 2025; Accepted 26 December 2025
Available online 6 January 2026

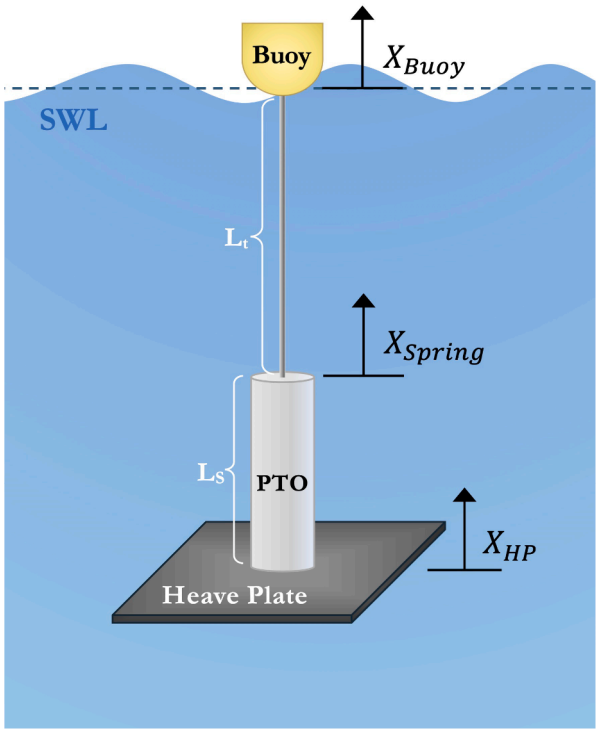

Fig. 1. Simplified representation of the main components of a two-body, heave plate WEC.

The dynamics of heave plate WECs have been investigated extensively through dynamic modeling and the development of oceangoing systems (Brown and Thomson, 2015; 4th Annual Marine Energy Technology Symposium , METS; Brown et al., 2017; Davis et al., 2014; Hamilton et al., 2014; Walker et al., 2025). These studies establish a strong foundation for advancing heave plate WEC modeling and design. Several offshore hydrodynamic interaction and WEC modeling tools are available, including WEC-Sim, WAMIT, and OrcaFlex (2nd Marine Energy Technology Symposium, 2014; Lee, 1995; Orcina, 2020). Building on the insights provided by these works, we have developed a dynamic model capable of efficiently exploring the complex parameter space inherent to heave plate WEC systems.

While comprehensive hydrodynamic interaction models and commercial tools provide high-fidelity analyses, they are computationally intensive. For applications requiring small-scale onboard energy harvesting, a simplified analytical model offers significant advantages. Our framework captures the essential dynamics while remaining computationally efficient and adaptable. This enables rapid parameter exploration, straightforward validation against experiments, and inclusion of additional physical processes, control strategies, or optimization routines. Traditional WEC development has relied on iterative, trial-and-error design refinement over extended timescales and has resulted in some suboptimal solutions (Bonfanti and Giorgi, 2022; Trueworthy and DuPont, 2020). By employing a lumped parameter model early in the design process, we can evaluate design options quickly and effectively.

This work details the development of the model and the configuration of the validation experiments. The model's parameter space is investigated with theoretical predictions compared to experimental dynamic responses. With these results we evaluate the model's accuracy and applicability.

2. System model

Many two-body WEC systems exploit wave-induced vertical motion differentials and generate power through rotational or translational mechanical devices. This study models the power take-off mechanism generically using an idealized spring-damper piston mechanism (Fig. 1).

The initial, unperturbed vertical position reference frame of the buoy, spring and heave plate are each represented with X_{Buoy}, X_{Spring}, and X_{HP}. The dashed line marks the still water line (SWL). Here initial unstretched spring length is L_S and the tether length is L_t. The appropriate tether length (L_t) is determined by the design's target sea state. This nonrigid tether may transition between taut and slack and connects the buoy to the top of the spring. It is only able to provide a positive, tensile vertical force on the spring.

As the target application for this system is to provide power for small (1 to 2 m long) UUVs, we consider wave conditions relevant to this scale. Wave heights can vary greatly, depending on location and wind conditions, but 'background' conditions of $O(1)$ to $O(10)$ s periods are omnipresent for most oceans, with corresponding deep-water wavelengths ranging from $O(1)$ to $O(100)$ m (Semedo et al., 2011; Caires et al., 2005). For the scale vehicle of interest, relevant wave scales include wavelengths of about 1 to 40 m and periods ranging from 1 to 5 seconds. According to linear wave theory (Eqn. 1), the orbital velocity of waves with periods of 1 to 5 s decay significantly (e^{-1}) at a depth roughly 4 to 10 m. In this analysis, we assume the heave plate is positioned within this practical vertical separation range and that wave-induced orbital motions are negligible.

Additionally, the idealized model considers an ideal buoy that follows surface motion exactly. The equivalent WEC surface buoy considered in our analysis behaves as a perfect tracker of local surface elevation in the wave frequency band of interest. Therefore, the connection to the tether is modeled as following the free surface.

This idealization isolates heave plate dynamics without resolving the transfer function associated with buoy mass, geometry, or radiation effects. By prescribing the surface motion directly, we neglect buoy dynamics and assume that the kinematic forcing to the PTO is not significantly altered by the coupled buoy-PTO-heave-plate system. This approximation can be considered suitable for buoys that are large relative to the heave plate buoyancy but small enough to respond to short-period seas such that hydrostatic forcing dominates (Falnes, 2002). However, it can break down for larger buoyancy systems or more energetic sea states and in those cases, more consideration should be given to buoy response. This assumption allows us to use the induced buoy excitation as a proxy for wave period (T_o) and height (H_o), which are referenced throughout.

2.1. Governing equations

Variables constraining the modeled spring-damper system are defined in Fig. 1. The deformation of the spring is determined from the relative motion between the top of the spring, X_{Spring}, and the heave plate position, X_{HP}, given as $\delta X = X_{Spring} - X_{HP}$. For the case shown in Fig. 1, in the unperturbed system $X_{Spring} = 0$ and $X_{HP} = 0$, thus $\delta X = 0$. The surface float experiences force induced by oncoming waves. The vertical motion is transmitted to the heave plate through the PTO spring and damper forces, F_K and F_C, respectively. In modeling the wave energy converter, we adopt a nonlinear damping formulation to account for velocity-dependent hydrodynamic forces, consistent with Bailey and Bryden (2012) and with our physical model described further below. Therefore, the damping force is proportional to the spring deformation rate ($\delta\dot{X}$) squared.

$$F_{PTO} = F_K + F_C = K_{PTO}\delta X + \hat{C}_{PTO}\delta\dot{X}|\delta\dot{X}| \tag{2}$$

where K_{PTO} is the linear spring constant and $\hat{C}_{PTO}$ is the quadratic damping coefficient characteristic of the modeled PTO. The theoretical power available for the WEC is approximated using the power dissipated by damping $P = F_C\dot{X}$ which assumes 100% efficiency. The actual power available will depend on the efficiency of the PTO which is not resolved in this idealized model. F_{PTO} drives the motion of the submerged heave plate.

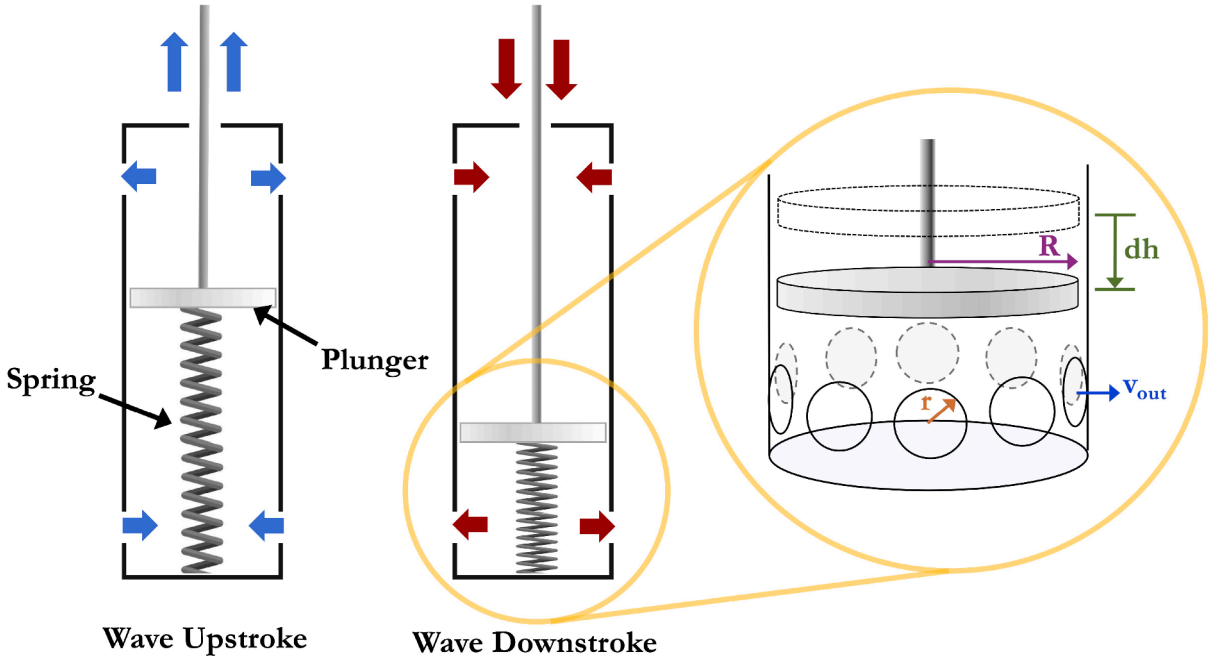

Fig. 2. Schematic of the Wave Energy Piston (WEP) on the upstroke and downstroke of a wave. Magnified view of the radially oriented damping outlet holes with the relevant geometries labeled.

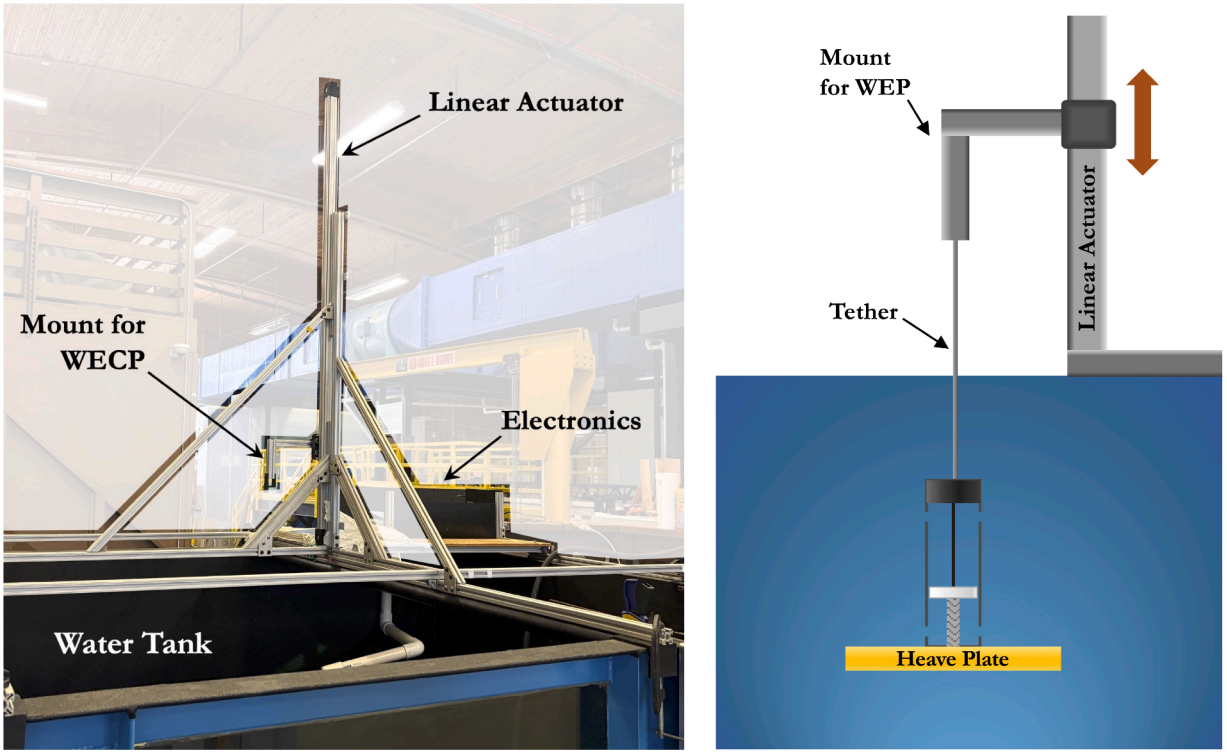

Fig. 3. (Left) Annotated lab setup for WEP testing. (Right) Schematic of the testing setup with underwater view of the WEP connected to the linear actuator mount.

The heave plate is also subject to both drag and inertial forces. The resulting motion is governed by the Morison equation, which captures the effects of accelerating a submerged body through a fluid (Morison et al., 1950).

$$F_{Mor} = F_D + F_{AM} = C_D \frac{1}{2} A \dot{X}_{HP} |\dot{X}_{HP}| + C_M M \ddot{X}_{HP} \tag{3}$$

where F_D is form drag and F_{AM} is added mass force. Here, C_D is the drag coefficient, A is the area, $\dot{X}_{HP}$ is the heave plate velocity, C_M is the added mass coefficient, M is the mass of the heave plate and associated components. The heave plate is modeled as a thin, square flat plate.

Drag and added mass forces vary greatly depending on the plate geometry and the frequency and amplitude of the oscillatory motion (Gar et al., 1958). Gar et al. (1958) and 4th Annual Marine Energy Technology Symposium (METS) examined C_D and C_M for several plate geometries as a function of the Keulegan-Carpenter (KC) number. For a plate

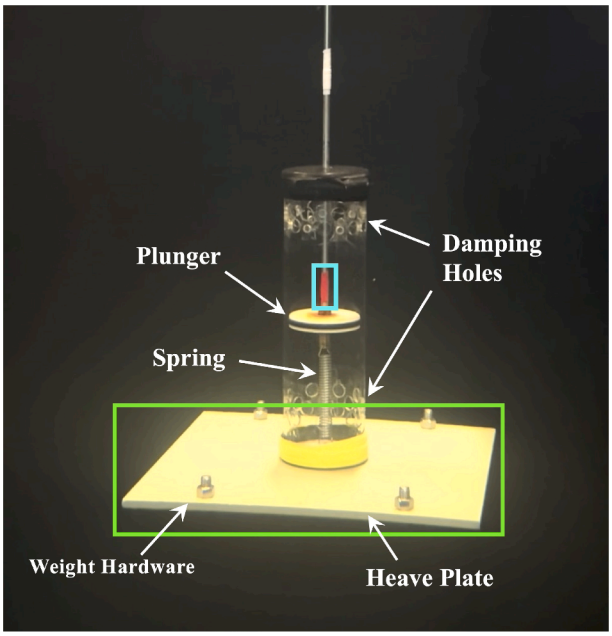

Fig. 4. View of the submerged WEP with components annotated. The bright green and blue boxes surrounding the heave plate and plunger, respectively, represent the WEP components that were tracked during video analysis. (For interpretation of the references to colour in this figure legend, the reader is referred to the web version of this article.)

oscillating in a fluid, this is defined as

$$KC = \frac{U_m T}{L}$$

where U_m is the maximum velocity of the oscillating plate, T is the period of oscillation, and L is a characteristic length, which in the case of a heave plate can be its width or its horizontal length. For the KC numbers expected in our applications, C_D for flat plates range between 4 and 10 and C_M between 1 and 3. In our analysis, we use constant C_D and C_M values (Appendix A.1).

Lastly, we consider the gravitational force, represented using reduced gravity which accounts for buoyancy acting on the heave plate.

$$F_g = Mg\frac{(\rho_{HP} - \rho_w)}{\rho_{HP}} \tag{4}$$

ρ_{HP} is the heave plate density, ρ_w is seawater density, and g is gravitational acceleration. The motion of the heave plate is then described by the force balance, given as

$$M\ddot{X}_{HP} = F_g + F_{Mor} + F_K + F_C \tag{5}$$

The expanded formula is

$$M\ddot{X}_{HP} = Mg\frac{(\rho_{HP} - \rho_w)}{\rho_{HP}} + C_D\frac{1}{2}A\dot{X}_{HP}|\dot{X}_{HP}| + C_M M\ddot{X}_{HP} + K_{PTO}\delta X + \hat{C}_{PTO}\delta\dot{X}|\delta\dot{X}| \tag{6}$$

The resulting dynamics are influenced by a variety of parameters that have a substantial impact on the performance of the system. These parameters include physical features such as the geometry of the heave plate, the mass of the system, and the PTO properties, as well as the frequency and amplitude of surface waves. We therefore require a robust and comprehensive understanding of the system's dynamics under different operating conditions.

3. Parameter scaling

We conducted a series of experiments to validate the model, varying key system characteristics including mass (M), spring constant (K_{PTO}), and quadratic damping coefficient ($\hat{C}_{PTO}$). These parameters are non-dimensionalized using characteristic dynamic scales of the system and include the wave height (H_o), wave time scale or wave period (T_o), and the cross-sectional heave plate area (A).

To scale mass, we relate the reduced gravity and drag force.

$$\frac{\rho_{HP} - \rho_w}{\rho_w} \forall g = 0.5 C_D U^2 A \tag{7}$$

Here, $\forall$ is the heave plate volume, C_D is the drag coefficient, U is the falling velocity, and A is the heave plate area. Rearranging 7 we find the terminal velocity from the force balance .

$$U = \left(\frac{\rho_{HP} - \rho_w}{0.5\rho_w C_D A} \forall g\right)^{0.5} \tag{8}$$

We consider the case where the terminal velocity matches a characteristic vertical wave velocity scale obtained using the wave length and time scales, H_o and T_o.

$$\frac{H_o}{T_o} = \left(\frac{\rho_{HP} - \rho_w}{0.5\rho_w C_D A} \forall g\right)^{0.5} \tag{9}$$

A reference mass calculated as $M_o = (\rho - \rho_w)\forall g$ from the comparison between the terminal velocity and the wave velocity scale. Eq. 9 can be rearranged for a relationship for the reference mass

$$M_o = 0.5\frac{H_o^2}{gT_o^2}\rho_w C_D A \tag{10}$$

Thus, scaled mass is the reduced mass of our system divided by the reference mass $M^* = M/M_o$. Using harmonic oscillator definitions, the spring constant K_{PTO} is scaled in terms of the wave forcing time scale and reference mass (Kreyszig, 2011). For a harmonic system, the reference spring constant is dependent on T_o and M_o.

$$K_o = \left(\frac{2\pi}{T_o}\right)^2 M_o \tag{11}$$

The non-dimensional spring constant ratio is therefore $K^* = K_{PTO}/K_o$. The quadratic damping factor (C_o) is defined in terms of the wave forcing length and reference mass scales (Goering, 1967).

$$C_o = \frac{M_o}{H_o} \tag{12}$$

We are left with a non-dimensional quadratic damping factor of $\hat{C}^* = \hat{C}_{PTO}/C_o$.

4. Experimental setup

For the validation experiments, the idealized spring-damper PTO was represented using a submersible piston model (Fig. 2). The physical prototype utilizes the heaving motion of a surface float to drive a piston plunger, cyclically reducing and expanding a control volume. The resulting flow induced by the plunger displacement serves as a proxy for the available power. The piston response was evaluated under varying simulated wave conditions in a laboratory setting, where experimental data were used to validate and refine the model.

4.1. Piston design and power

The Wave Energy Piston (WEP) consisted of a clear acrylic cylinder measuring 3.8 cm in radius and 30.5 cm in length (Fig. 2). A fiberglass heave plate was mounted at the base of the cylinder and can be interchanged to modify the cross-sectional area and mass of the system. In the experiments presented here, the heave plate area was fixed at 0.1 m^2. A central plunger, attached to a guide rod, oscillates vertically and drives water through a set of radially oriented holes located at both the top and bottom ends of the cylinder. There were 16 holes on each end, each with a 0.64 cm radius. When fluid passes through an orifice, it contracts and behaves as though it is flowing through a smaller effective opening. For

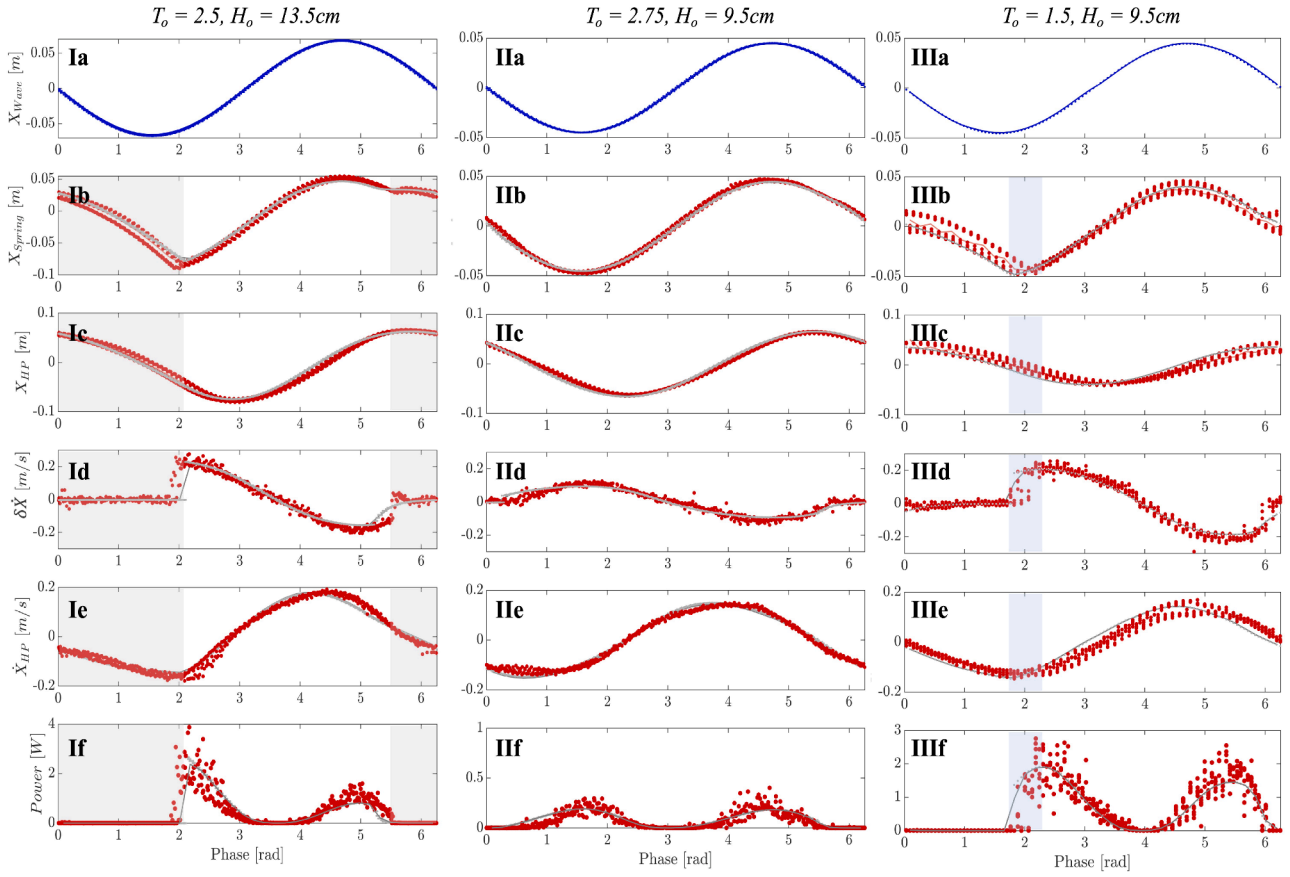

Fig. 5. Phase-averaged wave forcing (blue), model (gray) and experiment results (red) for a 13.5 cm, 2.5 second wave (Ia-f), a 9.5 cm, 2.75 second wave (IIa-f), and a 9.5 cm, 1.5 second wave (IIIa-f). The simulated wave forcing (I,II,IIIa), spring (I,II,IIIb) and plate (I,II,IIIc) position, spring (I,II,IIId) and plate (I,II,IIIe) velocity, and power (I,II,IIIf). In the left panels (Ia-f), gray blocks denote the phases in which the spring is fully retracted. On the right panels (IIIa-f), blue-gray blocks mark phases where there is a snap load. (For interpretation of the references to colour in this figure legend, the reader is referred to the web version of this article.)

a blunt edged orifice this was accounted for in a coefficient of discharge of 0.63, making the hole radius in our application effectively 0.51 cm (J. D. Richetta, 1937).

The damping coefficient ($\hat{C}_{\mathrm{PTO}}$) was adjusted by changing the number of open holes, thereby controlling the effective area for water inflow and outflow. Increasing damping involves covering more holes to reduce the available flow area. The volumetric flow through the open holes was used as a proxy to estimate the power available from the system. The spring constant (K_{PTO}) was modified by replacing the internal spring of the WEP.

The relative motion between the simulated buoy forcing and heave plate motion moves the plunger and induces an internal flow when moved over a distance dh. For a time step dt, the rate of change in plunger height was represented by dh/dt (Fig. 2). For example, when the plunger fell, as shown in the yellow circled view in Fig. 2, water was pushed out of the small radially oriented holes at the bottom of the piston and drew water in the holes at the top. The rate of change of volume inside the piston ($\dot{V}_{internal}$) and the outlet holes volume flow rate (Q_{Out}) are equal.

$$\dot{V}_{internal} = Q_{Out} \tag{13}$$

where $\dot{V}_{internal} = 2\pi R^2 \frac{dh}{dt}$ and $Q_{Out} = v_{out} n \pi r^2$. Substituting these definitions into Eq. 13 we can determine the velocity through damping holes v_{out} as

$$v_{out} = \frac{2}{n}\frac{R^2}{r^2}\frac{dh}{dt} \tag{14}$$

To estimate idealized power (P) from experimental results, we relate the time change in kinetic energy in terms of our problem geometry. We assume that kinetic energy in the outflow was available to the PTO so

$$P = \frac{1}{2}\rho v_{out}^2 Q_{Out} \tag{15}$$

Substituting the definition of Q_{Out} gives

$$P = \frac{1}{2}\rho v_{out}^2 n\pi r^2 v_{out} \tag{16}$$

Substituting Eq. 14 into 16 yields a final relationship for power in terms of $\frac{dh}{dt}$

$$P = \pi\rho\frac{4}{n^2}\frac{R^6}{r^4}\left(\frac{dh}{dt}\right)^3 \tag{17}$$

4.2. Actuated wave field

To simulate surface buoy excitation from waves, an Arduino-controlled stepper motor was programmed to move a linear actuator in mono- or multi-chromatic waveforms (Fig. 3). This forcing is consistent with an assumption of an ideal buoy that perfectly follows wave motion. The linear actuator simulated vertical wave motion with a tether connected to the WEP submerged in a 3 m wide by 2 m long by 1.5 m deep experimental tank. The actuator moved the WEP plunger via the connected tether (Fig. 3). This setup mimicked a realistic scenario in which the submerged WEP was pulled vertically by a surface buoy with the heave plate at a depth where the vertical wave motion has significantly decayed.

Wave height and frequency were adjustable and chosen to fall within a range of expected local wave conditions ($1 \leq T_o \leq 5$ sec and $0.04 \leq H_o \leq 0.33$ m) (Lindhart et al., 2024). During experiments, the vertical

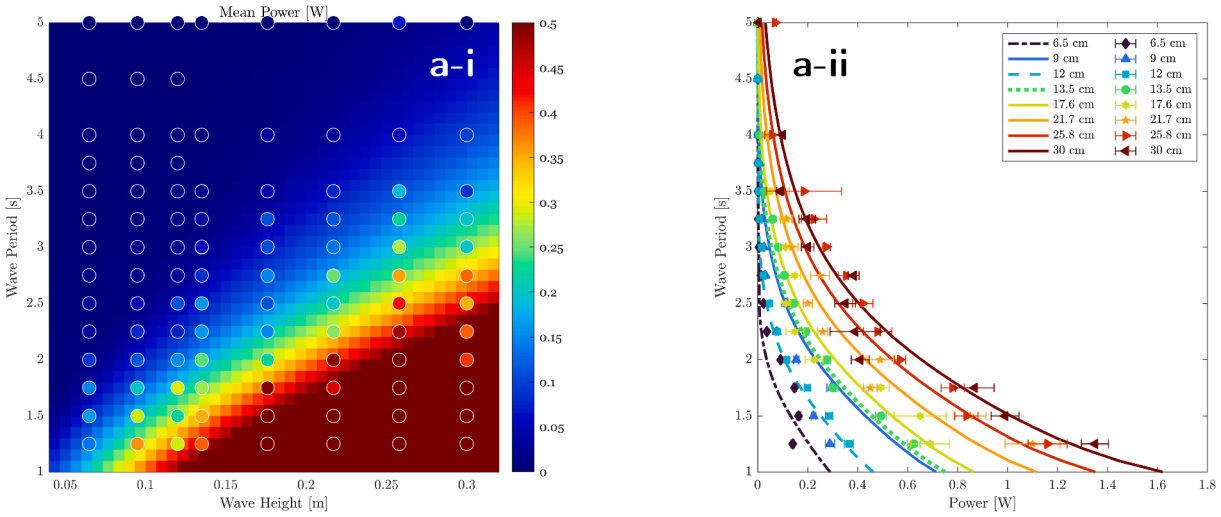

Fig. 6. (a-i) Modeled average power output for the WEP with $K^* = 30.4$, $\hat{C}^* = 25.2$, $A = 0.1m^2$ and $M^* = 1.48$ varying wave height and period. Corresponding estimated power availability for the WEP is marked in the white bordered circles. WEP parameters are scaled using central wave conditions evaluated, $H_o = 0.175\ m$ and $T_o = 2.5\ s$. (a-ii) Model and experimental power at the eight wave heights tested during experimentation. Wave period is aligned in (a-i) and (a-ii) for comparison.

position of the plunger and heave plate were determined using video recordings. Bright yellow and red tape markers on the heave plate and plunger respectively (Fig. 4) were tracked using MATLAB image processing. This produces $x-$ and $y-$pixel coordinates of the center of the tracked marker (The MathWorks, 2024). After calibration, pixel coordinates were converted to physical locations. From this, the rate of spring deformation (dh/dt) was calculated and used to estimate power availability (Eq. 17). This allowed us to compare the WEP performance with the model results under the same wave conditions.

5. Results

We compare the model predictions with experimental results to validate the lumped parameter model across the scaled parameter space. Building on this validated framework, we then identify ideal parameters for representative wave forcing conditions that maximize energy production.

5.1. Model validation

Fig. 5 shows the phase resolved model and experimental results for forcing waves of the following amplitude and period: 13.5 cm, 2.5 seconds; 9.5 cm, 2.75 seconds; and 9.5 cm, 1.5 seconds. In Fig. 5 the three wave cases are labeled I, II, and III in row a. In all cases, the WEP was configured with a fixed spring constant ($K_{PTO} = 220\ N/m$), quadratic damping coefficient ($\hat{C}_{PTO} = 165\ kg/m$), mass ($M = 1.75\ kg$), and area ($A = 0.1\ m^2$). The experimental power available was calculated using Eq. 17. The modeled and experimental dynamics aligned for all cases and captured complex features of spring-damper and heave plate interaction.

Notably, in the left column (Fig. 5 Ia-f), gray shading highlights a distinct change in the direction of the spring's motion. This occurred during the downstroke of the surface wave when the surface fell and the heave plate fell at a slower rate. In this case, the tether was slack and could not exert a force on the spring. The spring retracted to its original length (L_s), at a rate dependent on the K^* and $\hat{C}^*$, and moved with the heave plate until the surface wave began upward motion. The tether then became taut and pulled the spring upward. This feature was absent in column II. This exhibited the model's ability to capture the complex dynamics of the physical system in different regimes. Additionally, in the right column (Fig. 5 IIIa-f), blue shading highlights another complex dynamic feature. In this phase range, the heave plate and spring were falling and then were rapidly pulled up by the wave upstroke. This sharp transition resulted in a snap load and created a spike in power output (Fig. 5 IIIf). A snap load is a sudden transition between a slack and taut line resulting in a high-magnitude tensile force. In heave plate WEC applications, this typically occurs when the tether connecting the surface float and submerged mass becomes rapidly tensioned. Snap loads are undesirable dynamic responses and can damage mechanical systems (Niedzwecki and Thampi, 1991).

To validate our lumped parameter model across the parameter space, we conducted a series of experiments varying wave conditions and the WEP design parameters. We varied wave period and height between 1.25 to 5 seconds and 6.5 to 30 cm (Fig. 6). We saw an increase in power availability in the top panel of Fig. 6 as the wave period decreased and the wave height increased. This was expected as the power produced by the WEP increased with the spring deformation speed cubed. Therefore, larger waves with a short period stretched the spring quickly and produced greater power. The bottom panel of Fig. 6 provides a closer examination of power along the wave heights that were experimentally tested. For both experimental and model data, power increased nonlinearly as the wave period decreased.

Additional experiments were conducted to further explore the parameter space, varying the mass ratio of the WEP and the wave period (Fig. 7a). For these experiments, a base wave period T_o and wave height H_o of 2 seconds and 25.8 cm were used. The average power increased and then plateaued as M^* increased. With higher mass, spring deformation increased and greater force was required to move the heave plate, and therefore created a larger differential in motion between the surface element and the heave plate. This regime, combined with a decreased wave period, increased power.

Spring and damping PTO forces played a critical role in the performance of a WEC. To ensure the model accurately captured varying spring and damping force effects, additional validation tests were conducted by varying the non-dimensional spring and damping coefficients (K^* and $\hat{C}^*$) across waves of periods from 1.25 to 5 second waves. The power response as a function of spring stiffness and wave period revealed consistent trends in both the model and experimental data (Fig. 7b). The largest power was generated at low wave periods, and power output showed little sensitivity to increasing K^*. At lower spring constants ($50 \leq K^* \leq 400$), the power magnitude decreased, however, higher power was produced over a broader range of wave periods. When wave period and $\hat{C}^*$ varied, Fig. 7c showed that as wave period decreased and $\hat{C}^*$ increased, power also increased. However, only

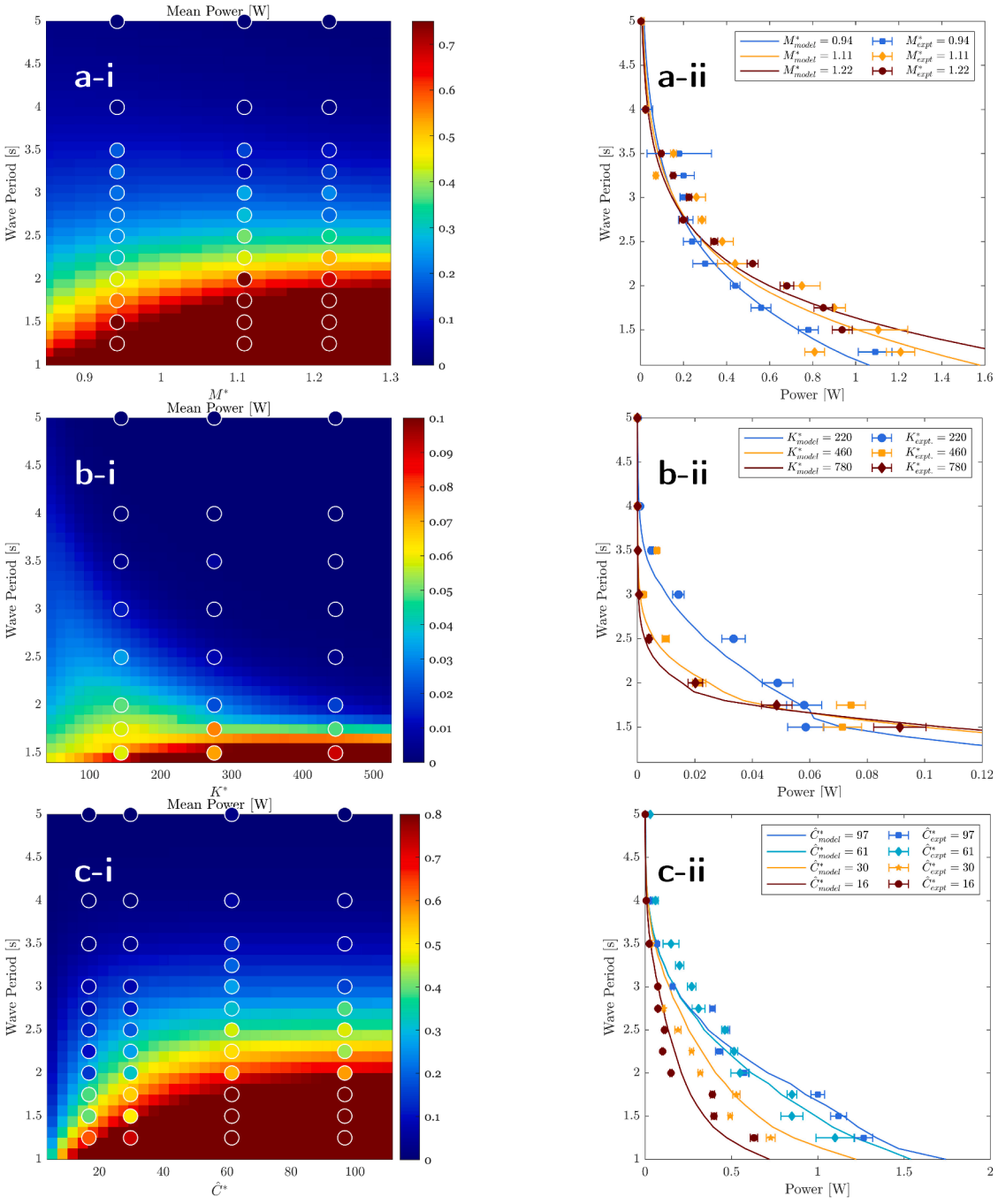

Fig. 7. In a,b,c-i, the estimated experimental power availability for the WEP is marked in the white bordered circles. (a-i) Model and experimental average power for a simulated $H_o = 0.258\ m$ with $K^* = 13.3$, and $\hat{C}^* = 16.2$ while varying WEP M^* and wave period. (a-ii) Model and experimental power at the three M^* values used during experimentation. (b-i) Modeled average power output for the WEP with $H_o = 0.065\ m$, $M^* = 5.1$, and $\hat{C}^* = 83.1$ varying wave period and K^*.(b-ii) Model and experimental power at the four masses tested during experimentation. (c-i) Modeled average power output for the WEP with $H_o = 0.205\ m$, $M^* = 0.91$, and $K^* = 21.2$ varying wave period and $\hat{C}^*$. (c-ii) Model and experimental power at the four masses tested during experimentation. For all cases, $T_o = 2.5\ s$ and $A = 0.1\ m^2$ are used in scaling.

marginal gains in power were observed with increased damping coefficients.

Spring and damping parameters are strongly coupled and jointly affect the power output of WEC systems. Subfigures 8a,b illustrated the combined influence of non-dimensional spring stiffness (K^*) and damping coefficient ($\hat{C}^*$) on power generation at two different wave periods. At a wave period of 1.5 seconds (Fig. 8a), the power output increased with higher $\hat{C}^*$ values, while variations in K^* have relatively little impact. For a 3.5 second wave period (Fig. 8b), in contrast, we saw a significant increase in power output at lower K^* and minimal impact on power output as $\hat{C}^*$ increased. These results support findings in Fig. 7b that a WEC with a lower K^* had a better broadband performance than higher K^*.

To further evaluate the accuracy of the model for more realistic conditions, a representative wave forcing time series was constructed based on averaged wave spectra recorded at Point Loma, CA (Fig. 9) (Lindhart et al., 2024). This averaged spectrum reflects the observed significant heights for wave periods corresponding to 1.4 to 20 seconds,

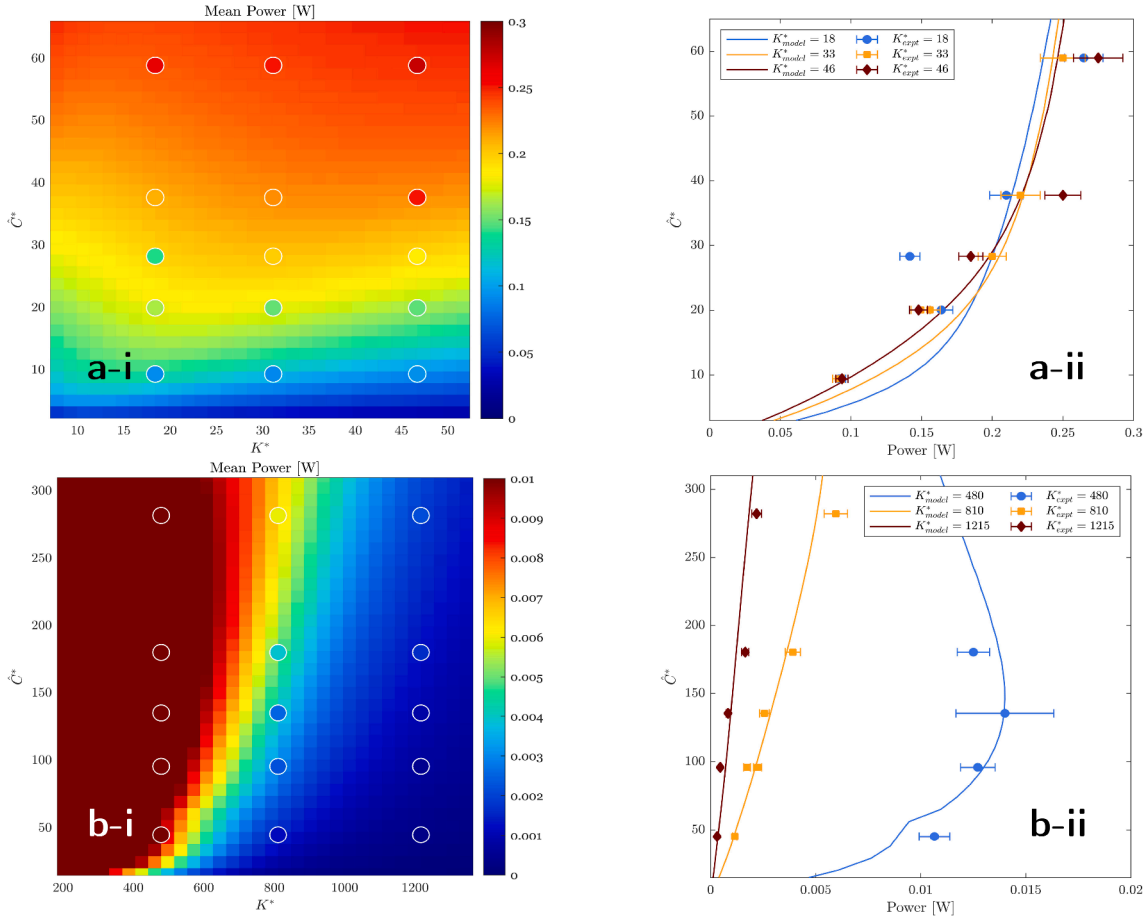

Fig. 8. (a-i,ii) Mean power as K^* and $\hat{C}^*$ are varied for a $T_o = 1.5\ s$, $H_o = 0.95\ m$ simulated regular wave. (b-i,ii) Mean power as K^* and $\hat{C}^*$ are varied for a $T_o = 3.5\ s$, $H_o = 0.95\ m$ simulated regular wave.

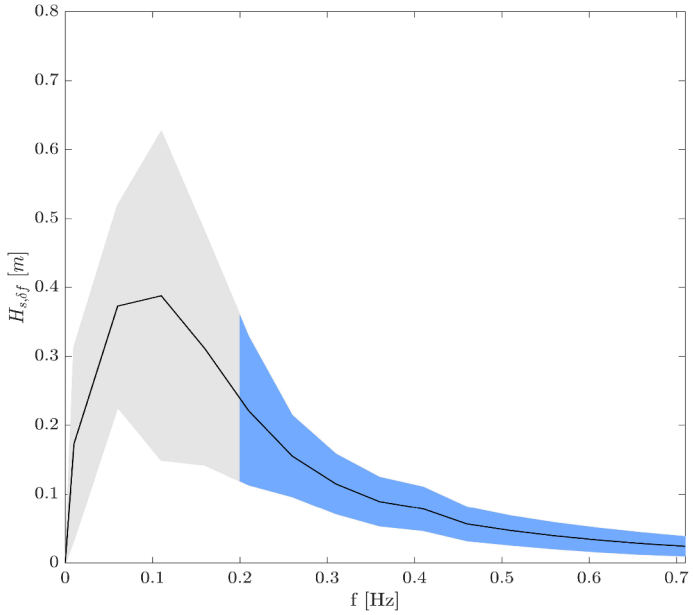

Fig. 9. Averaged frequency band significant wave height (black) versus wave frequency from Sofar Spotter buoy data collected in Pt. Loma, San Diego, CA Lindhart et al. (2024). The gray region represents 25 to 75% wave height quartiles. The blue region marks relevant wave frequencies for our applications. (For interpretation of the references to colour in this figure legend, the reader is referred to the web version of this article.)

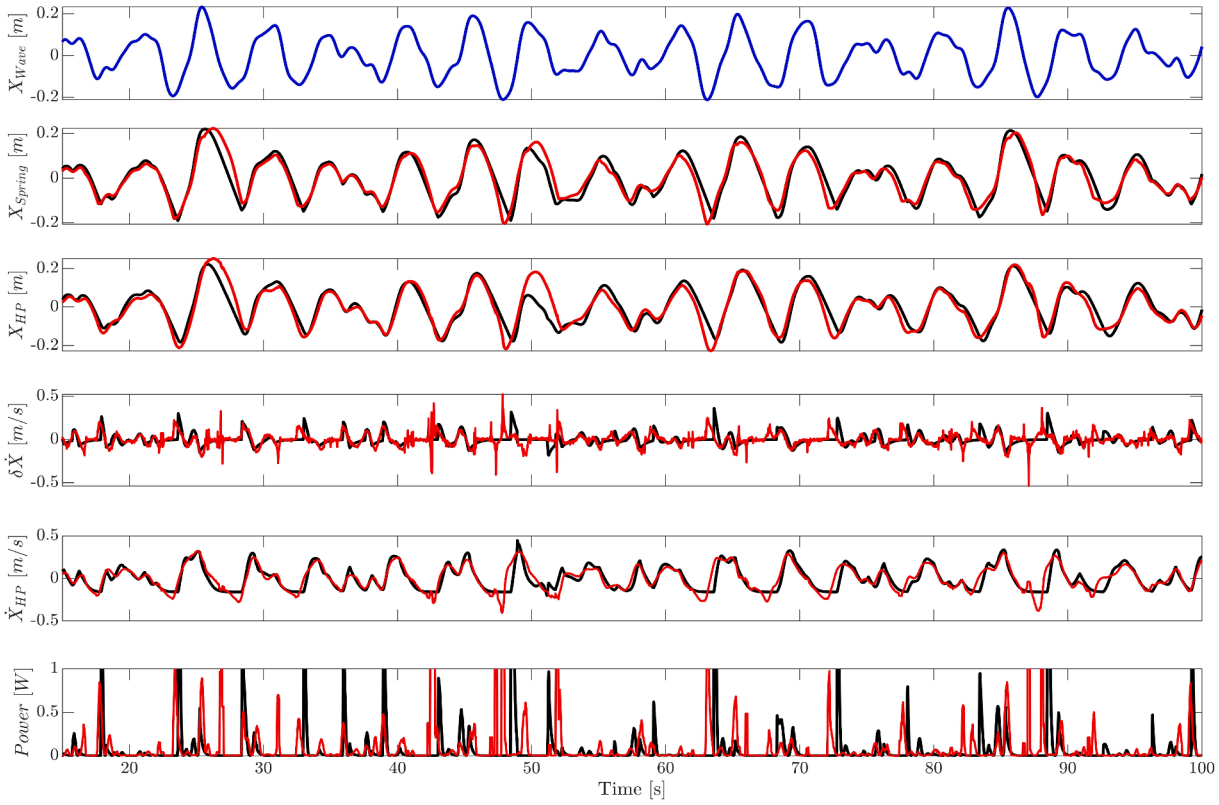

Fig. 10. Time series of modeled (black) and experimental (red) dynamics for realistic wave forcing. From top to bottom, panels show surface wave forcing, top of spring position, heave plate position, spring velocity, plate velocity, and power. (For interpretation of the references to colour in this figure legend, the reader is referred to the web version of this article.)

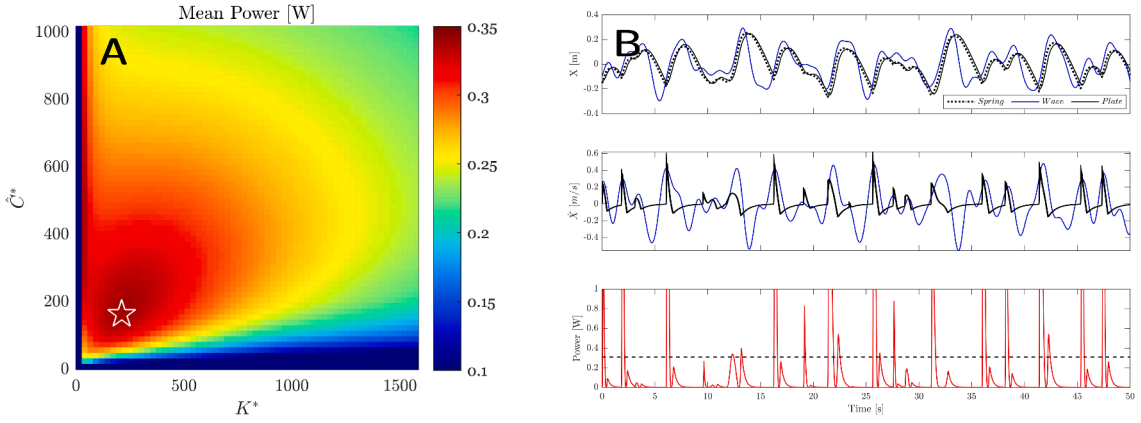

Fig. 11. (A) Modeled average power for irregular wave forcing when varying K^* and $\hat{C}^*$. Peak power is marked with a white star. (B) Time-resolved dynamics for the peak PTO parameter combination. The top panel shows the wave field, spring, and heave plate position series, the middle panel shows the wave field and spring velocities, and the bottom panel shows power time series (red) with the mean power marked (black dashed line). (For interpretation of the references to colour in this figure legend, the reader is referred to the web version of this article.)

approximately. This provided a realistic reference for sea states relevant to our application. The average spectrum was discretized into six dominant frequency components within the range of target wave periods for our application (1 to 5 seconds). These were then superimposed to generate a multi-frequency wave input for use in both simulations and physical experiments (Fig. 10). In general, the model-predicted response followed experimental measurements closely, demonstrating that the lumped parameter model reliably captured system dynamics under complex and irregular wave forcing. The averaged modeled power is 0.11 W (0.58 standard deviation) and the averaged experimental power available is 0.12 W (0.42 standard deviation). This result supports the model's applicability for performance prediction and control design in real-world sea conditions.

5.2. Model insights

Experiment and model comparisons across our parameter space indicated that the model performance was robust and can provide insight on ideal WEC designs to maximize power production in varying wave fields. We generated a discretized wave field using six harmonic components within the target wave field height and frequency range expected from recorded wave data in Fig. 9. Using this simulated time

series, we analyze the K^* and $\hat{C}^*$ parameter space to identify the ideal PTO characteristics for power generation in an irregular wave field. In these results, K^* and $\hat{C}^*$ were scaled using the period corresponding to the largest wave height component, thus T_o was 4 seconds and H_o was 0.22 m.

From Fig. 11, we found that the ideal K^* and $\hat{C}^*$ values were 211 and 165, respectively. At this PTO parameter combination the modeled power output was 0.35 W. As noted previously, this modeled power assumed 100% efficiency. With a micro hydropower turbine, the real efficiency would be between roughly 6 to 25% yielding an output power of 20 to 87.5 mW (Eliud et al., 2017; Khan et al., 2008). These results illustrated that the model can be a powerful tool when designing small WECs. This could be applied to determine ideal, power-maximizing designs for WECs onboard UUVs.

6. Discussion

Experiments demonstrate that our model effectively captured the complex dynamics of the WEP across a range of governing parameters H_o, T_o, M^*, K^*, and $\hat{C}^*$ under monochromatic wave forcing. Furthermore, simulations using realistic, irregular wave forcing showed strong agreement with experimental results, indicating the model's robustness and predictive power for expected wave conditions. The identification of optimal K^* and $\hat{C}^*$ combinations for WEP design highlights the model's practical value and applicability.

The validated model provides insights relevant to WEC development with UUV design considerations. Mass is critical to consider in WEC designs though optimal mass for WECs often contradicts ideal marine system design goals. UUVs are typically positively buoyant, however, for improved WEC capabilities the submerged mass must be negatively buoyant. Thus, balancing the two effects is essential and consideration must be taken if incorporating a heave plate WEC onboard of a marine vehicle. Varied mass versus wave period showed diminishing gains in mean power production at greater masses with negligible differences between $M^* = 1.1$ and $M^* = 1.3$ (Fig. 7(a-i,ii)). Considering this, a WEC designed for a UUV should fall closer to an $0.9 \leq M^* \leq 1.2$ in order to balance mass and power production benefits.

Another key takeaway from experiments is the influence of PTO spring constant on average power. Figs. 11(b-i,ii) and 8 showed that lower spring constants, despite having a lower peak power, had an improved broadband performance. This indicates that for a WEC operating in mixed sea states where energy is distributed across a range of frequencies, a lower K^* may be preferred.

As described earlier, the present model assumes the buoy follows the free surface exactly, neglecting the buoy's dynamic response to wave excitation. The response of a real buoy would impose a transfer function that filters and modifies the incident wave motion is transmitted to the PTO-heave-plate system. The omission of this transformation is a limitation of the current model and future work could incorporate a known buoy response to provide more realistic kinematic forcing.

Future model development should also include the implementation of time variable drag (C_D) and added mass (C_M) coefficients, which are currently treated as constants. Drag and added mass are frequency dependent and vary with phase for unsteady flow as well as with heave plate geometry. Therefore, incorporating their variability would enhance model fidelity. Additionally, the current model only accounts for vertical motion. During experiments there was additional movement in x and y axes which likely influenced the system performance. In the future this motion should be accounted for.

Finally, while the model provides a strong foundation for WEC design, mechanical durability must be addressed in future work. The present analysis does not consider material limits such as yield strength or the effects of snap loading, which are critical for ensuring long-term performance and structural reliability of WEC systems.

CRediT authorship contribution statement

Hannah Walker: Writing – original draft, Visualization, Methodology, Investigation, Formal analysis, Data curation; **Michael T. Tolley:** Writing – review & editing, Supervision, Funding acquisition, Conceptualization; **Geno Pawlak:** Writing – review & editing, Supervision, Methodology, Funding acquisition, Conceptualization.

Declaration of competing interest

The authors declare that they have no known competing financial interests or personal relationships that could have appeared to influence the work reported in this paper.

Acknowledgments

This work was funded by the ONR UCSD Naval Innovation, Science, and Engineering Center (NISEC) Fellowship N00014-23-1-2831 and by ONR MURI N00014-22-1-2595. Any opinions, findings, and conclusions or recommendations expressed in this material are those of the author(s) and do not necessarily reflect the views of the Office of Naval Research. We are grateful for comments from two anonymous reviewers that substantially improved the manuscript. This work builds upon preliminary work presented at the 2025 European Wave and Tidal Energy Conference (EWTEC) and included in the conference proceedings (Walker et al., 2025). This work benefitted from extensive conversations with the UCSD Environmental Fluid Dynamics Lab as well as the UCSD Bioinspired Robotics and Design Lab. The authors would also like to acknowledge the Scripps Institution of Oceanography Hydraulics Lab for allowing use of their facilities for these experiments.

Appendix A

A.1. Hydrodynamic coefficients

Drag and added-mass coefficients are defined as

$$C_D = \frac{2F_D}{\rho A \dot{X}_{HP}^2} \tag{A.1}$$

and

$$C_M = \frac{F_M}{\rho \forall \ddot{X}_{HP}} \tag{A.2}$$

Where F_D and F_M are the drag and added mass forces, ρ is the fluid density, A is the heave plate area, $\forall$ is the displaced volume, and $\dot{X}_{HP}$ and $\ddot{X}_{HP}$ are the velocity and acceleration of the heave plate. The characteristic length (L) of the plate was 0.33 m.

Values used in our model were obtained experimentally. To determine the drag coefficient, we initiated motion using a step function over a short distance, $L/2$, consistent with the ranges of simulated wave motion used in our model validation experiments. The plate was moved up and down at constant velocities (U) ranging from 5 to 20 cm/s. During motion, the force required to move the plate was recorded with a load cell.

After accounting for the initial acceleration transient within distance $L/3$ and buoyant and gravitational forces, mean drag force values for each velocity segment were fit to U^2 using a least-squares regression, yielding C_D to be 4 ± 1 (std. dev.). Consistent with findings by Johari and Stein (2002) and Grift et al. (2019), the plate drag was still evolving in the range tested, explaining the relatively large drag coefficient. This value represented drag well for the low vertical excursions ($< L$) in our experiments.

To identify the added mass coefficient C_M, the plate was accelerated over distance $L/3$ at a known rate ($0.6\ m/s^2$) and the corresponding force was recorded. After subtracting the buoyant, gravitational and drag force contributions, the remaining force was fit to (Eqn. A.2), resulting in $C_M = 2.5 \pm 0.75$ (std. dev.).

Although sensor noise and sampling variability contributed to the relatively large standard deviations, these coefficients resulted in good agreement for our validation experiments and fall within typical literature ranges for similar Reynolds and Keulegan Carpenter numbers (Gar et al., 1958).

References

2nd Marine Energy Technology Symposium, 2014. Development and demonstration of the WEC-Sim wave energy converter simulation tool.

4th Annual Marine Energy Technology Symposium (METS), 2016. Phase-resolved heave plate dynamics for wave energy converters, Washington D.C., USA. http://depts.washington.edu/pmec/docs/METS2016_Brown.pdf.

Bailey, H., Bryden, I., 2012. Influence of a quadratic power take-off on the behaviour of a self-contained inertial referenced wave energy converter. Proc. Inst. Mech. Eng., Part M: J. Eng. Maritime Environ. 226 (1), 15–22. https://doi.org/10.1177/1475090211425143

Bonfanti, M., Giorgi, G., 2022. Improving computational efficiency in WEC design: spectral-domain modelling in techno-economic optimization. J. Marine Sci. Eng. 10 (10), 1468. https://doi.org/10.3390/jmse10101468

Brown, A., Thomson, J., Rusch, C., 2017. Hydrodynamic coefficients of heave plates, with application to wave energy conversion. IEEE J. Oceanic Eng. PP, 1–14. https://doi.org/10.1109/JOE.2017.2762258

Brown, A.C., Thomson, J., 2015. Heave plate dynamics for a point absorbing wave energy converter. In: Proc. 3rd Marine Energy Technol. Symp, pp. 1–5.

Caires, S., Sterl, A., Gommenginger, C.P., 2005. Global ocean mean wave period data: validation and description. J. Geophys. Res.: Oceans 110 (C2). https://doi.org/https://doi.org/10.1029/2004JC002631

Cruz, J., 2007. Ocean wave energy: current status and future prespectives. Springer Science & Business Media.

Daniel, T., Manley, J., Trenaman, N., 2011. The wave glider: enabling a new approach to persistent ocean observation and research. Ocean Dyn. 61, 1509–1520. https://doi.org/10.1007/s10236-011-0408-5

Davis, A.F., Thomson, J., Mundon, T.R., Fabien, B.C., 2014. Modeling and analysis of a multi degree of freedom point absorber wave energy converter. In: International Conference on Offshore Mechanics and Arctic Engineering. Vol. 45509. American Society of Mechanical Engineers, p. V08AT06A046.

Eliud, K., Musembi, N.M., Kindole, D., Mukama, A., Kosgei, S.K., Nemoto, Y., Nakajo, Y., 2017. Study of performance characteristics of small submersible pump run as hydro turbine generator. Sustain. Energy 5 (1), 1–5. https://doi.org/10.12691/rse-5-1-1

Falnes, J., 2002. Ocean Waves and Oscillating Systems. Cambridge University Press. Chapter 5.6: The Froude-Krylov Force and Small-Body Approximation, pp. 160–183.

Falnes, J., 2007. A review of wave-energy extraction. Marine Struct. 20 (4), 185–201. https://doi.org/https://doi.org/10.1016/j.marstruc.2007.09.001

Gar KeuleganH., Carpenter, L.H., 1958. Forces on cylinders and plates in an oscillating fluid. J. Res. Natl. Bureau Standard. 60, 423. https://api.semanticscholar.org/CorpusID:124303029.

Goering, K.L., 1967. Transient Response of a Harmonic Oscillator with Quadratic Damping. Ph.D. thesis. Rice University.

Grift, E.J., Vijayaragavan, N.B., Tummers, M.J., Westerweel, J., 2019. Drag force on an accelerating submerged plate. J. Fluid Mech. 866, 369-398. https://doi.org/10.1017/jfm.2019.102

Guo, B., Wang, T., Jin, S., Duan, S., Yang, K., Zhao, Y., 2022. A review of point absorber wave energy converters. J. Marine Sci. Eng. 10 (10), 1534. https://doi.org/10.3390/jmse10101534

Hamilton, J.A., Henriques, J., Cazenave, F., McGill, P., Radochonski, W., Falcão, A., Gato, L., Gomes, R., 2014. Results from numerical simulation and field tests of an oceanographic buoy powered by sea waves. In: International Conference on Offshore Mechanics and Arctic Engineering. Vol. 45547. American Society of Mechanical Engineers, p. V09BT09A021.

J. D. Richetta, W.E.H., 1937. Derivation of coefficients of orifices. J. Franklin Inst. 223, 83–94. https://doi.org/10.1016/S0016-0032(37)90586-6

Johari, H., Stein, K., 2002. Near wake of an impulsively started disk. Phys. Fluids 14. https://doi.org/10.1063/1.1502267

Khan, M.I., Iqbal, M.T., Hinchey, M., 2008. Submerged water current turbines. In: OCEANS 2008, pp. 1–6. https://doi.org/10.1109/OCEANS.2008.5151891

Kreyszig, E., 2011. Advanced engineering mathematics-pdf. Bloomsbury Publishing.

Kundu, P.K., Cohen, I.M., Dowling, D.R., 2015. Fluid mechanics. Academic press.

Lee, C.H., 1995. WAMIT Theory Manual.

Lindhart, M., Daly, M.A., Walker, H., Arzeno-Soltero, I.B., Yin, J.Z., Bell, T.W., Monismith, S.G., Pawlak, G., Leichter, J.J., 2024. Short wave attenuation by a kelp forest canopy. Limnol. Oceanogr. Lett. 9 (4), 478–486. https://doi.org/https://doi.org/10.1002/lol2.10401

Morison, J.R., Johnson, J.W., Schaaf, S.A., 1950. The force exerted by surface waves on piles. J. Petrol. Technol. 2 (05), 149–154.

Niedzwecki, J.M., Thampi, S.K., 1991. Snap loading of marine cable systems. Appl. Ocean Res. 13 (1), 2–11. https://doi.org/10.1016/S0141-1187(05)80035-5

Falcão, A.F.d.O., 2010. Wave energy utilization: a review of the technologies. Renew. Sustain. Energy Rev. 14 (3), 899–918.

Orcina, 2020. OrcaFlex-Documentation, 10.1b Edition. Available online: https://www.orcina.com/releases/orcaflex-101/ (accessed on 23 June 2025).

Pinkel, R., Goldin, M., Smith, J., Sun, O., Aja, A., Bui, M., Hughen, T., 2010. The wirewalker: a vertically profiling instrument carrier powered by ocean waves. J. Atmos. Oceanic Technol. 101220134036059. https://doi.org/10.1175/2010JTECH805.1

Rehman, S., Alhems, L.M., Alam, M.M., Wang, L., Toor, Z., 2023. A review of energy extraction from wind and ocean: technologies, merits, efficiencies, and cost. Ocean Eng. 267, 113192.

Salter, S.H., 1974. Wave power. Nature 249, 720–724. https://doi.org/10.1038/249720a0

Semedo, A., Sušelj, K., Rutgersson, A., Sterl, A., 2011. A global view on the wind sea and swell climate and variability from ERA-40. J. Climate 24. https://doi.org/10.1175/2010JCLI3718.1

The MathWorks, I., 2024. Image Processing Toolbox. Natick, Massachusetts, United State. https://www.mathworks.com/products/image-processing.

Trueworthy, A., DuPont, B., 2020. The wave energy converter design process: methods applied in industry and shortcomings of current practices. J. Marine Sci. Eng. 8 (11), 932. https://doi.org/10.3390/jmse8110932

Walker, H., Tolley, M.T., Pawlak, G., 2025. Modeling and validation of a small-scale wave energy converter for unmanned underwater vehicle applications. Proc. Eur. Wave Tidal Energy Conf. 16. https://doi.org/10.36688/ewtec-2025-726